GDCh

Research Articles

Angewandte Chemie
International Edition
www.angewandte.org

Check for updates

Heterogeneous Catalysis

In Situ Formation of Platinum-Carbon Catalysts in Propane Dehydrogenation

Hannah C. Nerl[#], Milivoj Plodinec[+], Thomas Götsch,* Katarzyna Skorupska, Robert Schlögl, Travis E. Jones[++], and Thomas Lunkenbein*

Abstract: The catalytic production of propylene via propane dehydrogenation (PDH) is a key reaction in the chemical industry. By combining *operando* transmission electron microscopy with density functional theory analysis, we show that the intercalation and ordering of carbon on Pt interstitials to form Pt–C solid solutions is relevant for increasing propylene production. More specifically, we found that at the point of enhanced propylene formation, the structure of platinum nanoparticles is transformed into a transient caesium chloride-type Pt–C polymorph. At more elevated temperatures, the zincblende and rock salt polymorphs seemingly coexist. When propylene production was highest, multiple crystal structures consisting of Pt and carbon were occasionally found to coexist in one individual nanoparticle, distorting the Pt lattice. Catalyst coking was detected at all stages of the reaction, but did initially not affect all particles. These findings could lead to the development of novel synthesis strategies towards tailoring highly efficient PDH catalysts.

[*] Dr. H. C. Nerl,[#] Dr. M. Plodinec,[+] Dr. T. Götsch, Dr. K. Skorupska,
Prof. Dr. R. Schlögl, Dr. T. E. Jones,[++] PD Dr. T. Lunkenbein
Department of Inorganic Chemistry
Fritz-Haber-Institut der Max-Planck-Gesellschaft
Faradayweg 4–6, 14195 Berlin, Germany
E-mail: goetsch@fhi-berlin.mpg.de
        lunkenbein@fhi-berlin.mpg.de

Prof. Dr. R. Schlögl
Department of Heterogeneous Reactions
Max Planck Institute of Chemical Energy Conversion
Stiftstraße 34–36, 45470 Mülheim a.d. Ruhr, Germany

[#] now at: Department of Physics, Humboldt University of Berlin,
Berlin, Germany

[+] now at: Department of Chemistry and Applied Biosciences, ETH
Zurich, Zurich, Switzerland

[++] now at: Theoretical Division, Los Alamos National Laboratory, Los
Alamos, USA

Introduction

The heterogeneously catalyzed non-oxidative dehydrogenation of light alkanes to more reactive olefins is a key reaction in the chemical industry. One such example is the synthesis of propylene from propane. Propylene is a basic building block of a large variety of chemicals, including polypropylene and propylene oxide. The annual demand for propylene was estimated to be 114 million tons in 2019 and is projected to continue to grow.[1,2] Today, propylene is already produced commercially via the heterogeneously catalyzed process of propane dehydrogenation (PDH) over modified Pt-based catalysts[1] as it represents an efficient alternative to the more energy-demanding process of steam cracking.[3]

Generally, PDH is considered to have a relatively low reaction rate, even at industrial reaction conditions and its productivity is limited by low catalyst selectivity and short lifetime.[3] Coke formation on the surface of the catalyst during PDH leads to premature deactivation.[1,4] Regeneration cycles and the (*in situ*) formation of alloys between the catalytically active noble metal and a heteroelement, such as Zn, In, Mn or Sn has been considered a key strategy to enhance the productivity of PDH catalysts.[1,3,4b,5,6] Bulk alloying alters the surface geometry and the electronic structure of the catalyst, increasing selectivity of the dehydrogenation product and decreasing coke formation.[6–9]

To date, little is known about the bulk chemistry that occurs during the non-oxidative dehydrogenation of hydrocarbons using Pt catalysts. Aside from the obvious economic and environmental benefits of improving industrial propylene production,[10] understanding the structure that forms under working conditions will offer deep insights into how solid-state chemistry affects catalytic productivity.

The dissolution of carbon into the bulk of the catalyst has been shown to play a pivotal role in driving selectivity in catalytic hydrogenation[11] and n-hexane dehydrogenation[12] reactions. In Ni catalysts, for instance, coke formation and bulk chemistry have been shown to be inherently related.[13] Using high resolution transmission electron microscopy (HRTEM) it was also shown that carbon accumulates on interstitial sites in Au nanoparticles (NPs)[11a] and Ni₃Zn intermetallics[14] in hydrogenation reactions. For dehydrogenation reactions, the presence of dissolved carbon in the crystal structure was found to increase the catalytic performance.[11a,14] For example, it was found that the temperature-dependent bulk carbon content can greatly influence the selectivity of Pt catalysts.[12] However, details

Angew. Chem. Int. Ed. **2024**, *63*, e202319887 (1 of 9)

© 2024 The Authors. Angewandte Chemie International Edition published by Wiley-VCH GmbH

of the working structures of Pt-based catalysts, which are widely used in these reactions, remain elusive.

Here, we employ *operando* TEM to identify and correlate carbon ordering on interstitial sites of Pt NPs with propylene production in the industrially relevant endothermic reaction of PDH. Structural information was obtained *in situ* using selected area electron diffraction (SAED) and HRTEM imaging conducted under reaction conditions while simultaneously monitoring the catalytic activity using mass spectrometry (MS). Using density functional theory (DFT) calculations, we found that the presence of ordered Pt–C solid solutions can enhance the formation of propylene. The consequences for balancing the carbon content within the Pt nanoparticle for propylene productivity and coking will be discussed.

Results

Operando TEM Investigation

First, the structural evolution and temperature dependency of Pt NPs was studied during PDH using an *operando* TEM approach. Using online mass spectrometry (Figure S3), we monitored the conversion of propane to propylene (Figure 1) while simultaneously acquiring SAED during the temperature ramp to 600 °C (Figure 2). Proof of pr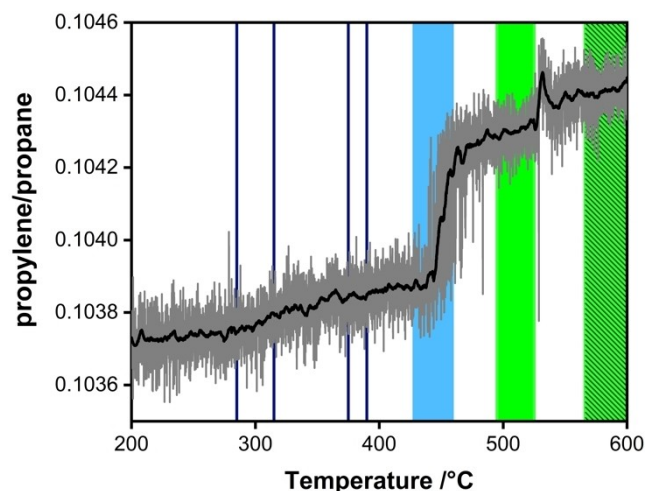opylene production is shown by the jump in the propylene-to-propane ratio during the temperature ramp that occurred between 438 °C and 474 °C. Above this temperature the propylene-to-propane ratio levelled off at higher values implying that a slight deactivation occurred or that the chemistry of the catalyst had changed.

The analysis of the diffraction information obtained *in situ* during the temperature ramp using SAED is shown in Figure 2. Additional reflections were observed in the SAED at 600 °C (Figure 2b) under PDH conditions that were absent at 280 °C (Figure 2a). At 600 °C, the main reflections (Figure 2b, blue circles) correspond to face-centred cubic (fcc) Pt NPs. In addition, a new reflection appeared at $d^{-1} = 0.61 \, \text{Å}^{-1}$, corresponding to a lattice spacing of 1.64 Å (Figure 1b, yellow circles). This new reflection does not correspond to metallic Pt. Instead, it can be assigned to lattice planes of different Pt–C structures (Figure 2d, Figure S4, and Table S1), such as ZnS-type (1.67 Å, 022, F-43 m, ICSD no. 1018164), NaCl-type (1.58 Å, 022, Fm-3 m, ICSD no. 1018165) and CsCl-type (1.63 Å, 111, Pm-3 m, ICSD no. 1002228).

In order to relate the formation of this additional reflection to the function of the catalyst, we acquired a series of SAED patterns during the temperature ramp to reaction conditions while measuring the conversion. The line profiles of the SAED patterns acquired *in situ* and details on the analysis are presented in the Supporting Information (Figure S5–S7). A contour plot showing reflections that can be assigned to the Pt–C crystal structures is shown in Figure 2c. The SAED pattern of the catalyst showed a complex and highly fluctuating dependence on temperature. Below 375 °C, the contributions of ordered Pt–C structures were found to be low. In the temperature regime between 375 °C to 390 °C, a broad intensity distribution around $0.58 \, \text{Å}^{-1}$ (1.72 Å) appeared, which shifted towards $0.60 \, \text{Å}^{-1}$ (1.67 Å) at higher temperatures suggesting the presence of ZnS-type and CsCl-type structures, respectively. At this point the propylene production increased slightly as shown in Figure 1. However, propylene production was still at an overall low level, most likely due to kinetic hindrance as a consequence of the low temperature. The presence of CsCl-type Pt–C polymorphs at relatively low temperatures is surprising from the chemistry point of view as this structure represents a substitutional polymorph, in which Pt atoms are removed from their original positions. This is generally accompanied by high activation barriers. This contrasts with the ZnS-type Pt–C polymorph, which is a diffusional structure, i.e. carbon is diffusing through the Pt lattice. Above 428 °C, the broad intensity peaks shift towards $0.60 \, \text{Å}^{-1}$ (1.67 Å), attributed to the CsCl-type polymorph. At 450 °C, the intensity of the $0.60 \, \text{Å}^{-1}$ (1.67 Å) contribution was found to be significantly increased (Figure 2b). This increase in intensity occurred at the same time as propylene production increased significantly (Figure 1). Above 474 °C, propylene production levelled off, which can be attributed to the shift of the intensity to $0.58 \, \text{Å}^{-1}$ (1.72 Å) implying that the ZnS-type polymorph is dominating in that regime. Between 570 °C and 600 °C the increase in temperature was not found to enhance propylene production significantly. However, an additional sharp reflection at ~$0.62 \, \text{Å}^{-1}$

Figure 1. Qualitative catalytic reaction traces for PDH over Pt NPs measured during the *operando* TEM experiment. The MS data shows that the propylene/propane ratio changed during the temperature ramp from 200 °C to 600 °C. The increase in the propylene/propane ratio at temperatures between 438 °C and 474 °C indicates increased production of propylene. Intervals highlight the temperature regimes in which SAED patterns have been recorded for structure-function analysis. The colour code of the filled intervals denotes the appearance of different Pt–C polymorphs and is adopted from Figure 2c. Blue filled regions denote the occurrence of the CsCl-type, filled pale green intervals correspond to the occurrence of the ZnS-type, and the striped area represents regimes in which ZnS-type and NaCl-type Pt–C polymorphs coexist. The trend of the traces is represented by the smoothed black curve.
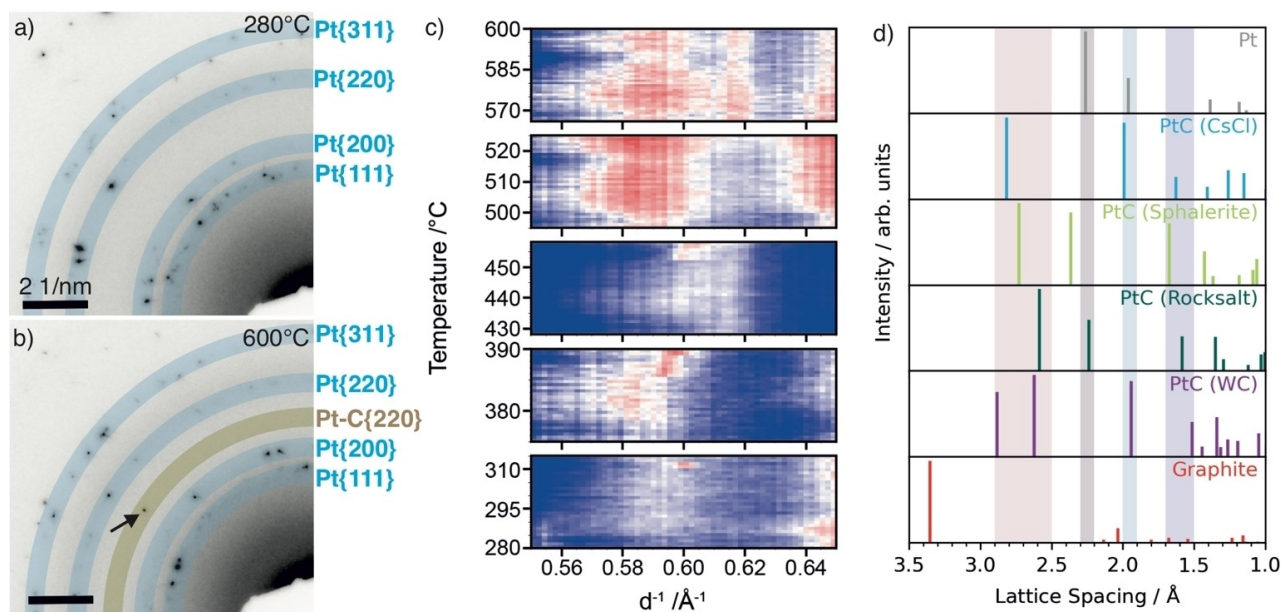
Figure 2. Structure analysis of Pt nanoparticles during PDH as obtained during *operando* TEM measurements. Selected area diffraction (SAED) recorded *in situ* at (a) 280 °C and (b) 600 °C during PDH. The blue circles highlight reflections that are expected for fcc-Pt, i.e. Pt (111), Pt (200), Pt (220), Pt (311) (from inside to outside). The yellow circle in b denotes distances matching Pt–C solid solutions. The arrows highlight the corresponding reflections. (c) Contour plots showing circularly integrated electron diffraction information between 0.55 Å^{-1} and 0.65 Å^{-1} (from b) for different temperature regimes: (280–315 °C, 375–390 °C, 428–459 °C, 495–525 °C, and 566–600 °C). The selected regions highlight lattice spacing ranges that are characteristic for unique reflections for CsCl (111)-, ZnS (220)-, and NaCl (220)-type crystal structures. Blue regions denote the background; diffraction signals are presented in white (low intensity) to red (high intensity). The graph in (d) shows the expected distances for Pt, different Pt–C structures, and graphite in reciprocal space for reference. The highlighted areas correspond to distances of 2.5–2.9 Å, 2.2–2.3 Å, 1.9–2.0 Å, and 1.5–1.7 Å in real space. Further details are presented in Figures S5–S7.

(1.61 Å) occurred. This new reflection could be assigned to a NaCl-type Pt–C polymorph coexisting with the ZnS-type Pt–C polymorph. The coexistence of polymorphs could indicate the presence of frustrated phase transitions in which carbon atoms are constantly diffusing onto different interstitial sites. The term "frustrated" refers to a situation in which the catalyst is held under conditions close to a thermodynamic phase transition where the two structures exhibit almost identical free energies.[15,16] Small local changes in the chemical potential can trigger the transformation from one structure to the other. Here, this is reflected in the ongoing interconversion of the ZnS-type to NaCl-type Pt–C polymorphs. The catalyst is thermodynamically frustrated and the system remains often trapped in a state of local instability. Furthermore, an increase of the integral width of the Pt–C reflections coincides with increased propylene production (shown in Figure S8).

To investigate the local chemistry of individual NPs, we recorded HRTEM images at 600 °C during operation (Figure 3a). NPs were found to be randomly oriented and exhibit different shapes, but mostly the NPs were rounded and not highly facetted. The averaged diffraction information shown in the Fast Fourier Transform (FFT) in Figure 3b indicates structural pluralism. In order to unravel different local structural contributions, we have calculated the inverse FFTs (IFFT) for different scattering vector ranges as shown in Figure 3c with individual contributions shown in Figure 3d–h. In IFFT analysis, the diffraction information

contained in the HRTEM images is utilized to map out the spatial distribution of specific reflections. The superposition in Figure 3c highlights that some NPs shown in the HRTEM image of Figure 3a did not feature lattice spacings in the selected range or contained no diffraction information. This is due to diffraction contrast being generated only when the crystal lattice is in specific orientations to the electron beam.

As shown in Figure 3e, only a small fraction of NPs were oriented such that lattice distances between 1.5 and 1.7 Å were observable. The range 1.9–2.0 Å corresponds to both, Pt (Pt (200)) and Pt–C structures (CsCl-type, (011); WC-type, (011)). Based on the number of particles visible in Figure 3f, the majority of the particles were in an orientation that allowed for imaging of these planes. These distances are absent in Pt–C of the ZnS- and NaCl- type. Only a few particles showed lattice distances between 2.2 and 2.3 Å (Figure 3g) which correspond to Pt NPs (Pt (111)) or to the {200} lattice planes of the NaCl-type Pt–C polymorphs. In Figure 3h, distances from 2.5 to 2.9 Å are shown—these are exclusively present in all four Pt–C structures (Figure 3a), but absent in metallic Pt and larger compared to the largest lattice planes expected for metallic Pt (Pt (111)). This increase in lattice distances would imply an expansion of the NPs during Pt–C formation far exceeding that expected due to thermal expansion.

During the temperature ramp, individual NPs also showed signs of coexistence of different Pt–C structures during PDH at 600 °C. As shown in the example in
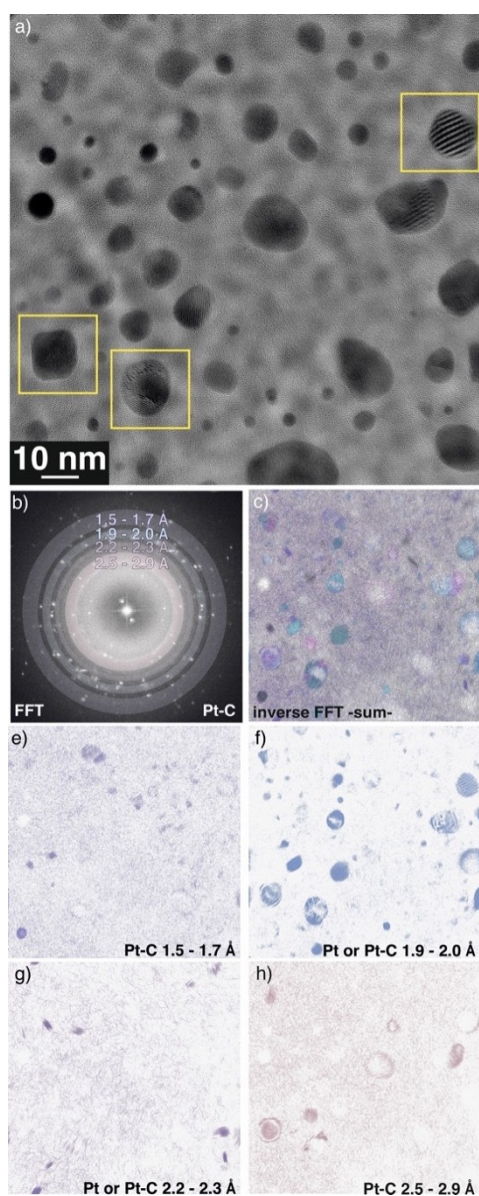
Figure 3. Presence of Pt–C containing NPs and enlarged lattice spacings in Pt NPs were observed during PDH after dwelling for 40 mins at 600 °C. (a) HRTEM image showing the rounded shape of the NPs at reaction conditions. Yellow boxes denote particles that are presented in Figure 4. (b) The corresponding Fast Fourier Transform (FFT) of the image shown in a. The coloured circular bands show positions from which various inverse FFT (IFFT) images were calculated and shown in e–h. (c) The image shows the superposition of the individual lattice plane contributions that are shown in e–h.

Figure 4a, on occasion two different structures appeared to coexist in individual NPs. Here, the lattice spacings were found to be increased to 2.75 Å and 2.10 Å. Carbon dissolution, diffusion and ordering into the bulk is known to increase the lattice spacing of NPs. Hence, this change in lattice spacing suggests the infiltration and intercalation of carbon into Pt. The increase to 2.75 Å can be assigned to the {111} lattice planes of a sphalerite (ZnS-type) Pt–C polymorph forming a sharp solid-solid interface. The observed
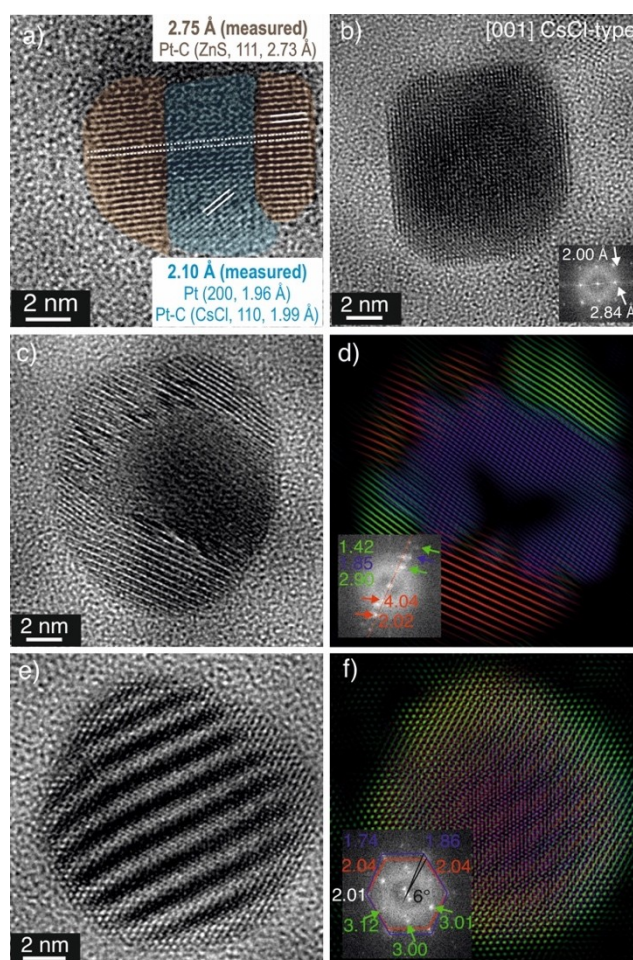

Figure 4. The coexistence of different Pt–C structures in one particle. (a) HRTEM image of a NP recorded after 40 mins at 600 °C showing lattice spacings that correspond to at least one Pt–C structure (annotations: brown = ZnS- type structure, blue = strained and distorted Pt or CsCl-type structures). The original image is shown in Figure S9. (b), (c), (e) TEM images of the regions marked in yellow in Figure 3a. The corresponding IFFT of the individual particles presented in (c) and (e) are placed in (d) and (f), respectively, demonstrating the spatial distribution of distances (in Å) given in the FFT insets. The colour code of the distance labelling within the FFT corresponds to the colour of the different lattice planes.

2.10 Å may correspond to heavily strained {200} and {110} lattice planes of fcc-Pt and CsCl-type Pt–C polymorphs, respectively. Since carbon diffuses easily between different Pt–C structures,[17] it is reasonable to expect that different Pt–C structures can coexist in one NP, giving rise to increased local complexity. In such a complex scenario, the solid-solid interface between the different Pt containing structures may act as diffusional gates for carbon to adjust and to promote the carbon content inside the Pt NP.[18] The complex nature of the NPs under reaction conditions is further shown in the analysis of representative, individual NPs from Figure 3a (marked in yellow). Figure 4b shows an example of a Pt–C NP that can be indexed to the [001] zone axis of the CsCl-type Pt–C polymorph, while the NP shown in Figure 4c is composed of at least three different crystals

as indicated by the IFFT analysis given in Figure 4d. The distances 2.90 Å and 2.02 Å can be assigned to a CsCl-type crystal structure, but the lattice plane distance of 1.85 Å does not match any spacings of known Pt–C structures. It may arise from a heavily strained (220) lattice plane of the ZnS-type Pt–C polymorph. Figure 4e displays a NP that exhibits a strong Moiré pattern. IFFT analysis of the image is shown in Figure 4f. It suggests the presence of a CsCl-type Pt–C polymorph (red) as well as a strained ZnS-type Pt–C polymorph with a 6° rotation between the regions. Note that the CsCl-type Pt–C polymorph appeared to be absent at a similar temperature in the SAED analysis (Figure 2) obtained during the temperature ramp. This may be due to the SAED averaging the information over a larger spatial region. The reflections at ~3.01 Å in Figure 4f suggest the presence of a third structure with a high carbon content. A shell of higher carbon-content appears to surround an otherwise saturated Pt–C core.

Thus, the observed differences in the lattice parameter can also stem from the presence of varying amounts of carbon of the interstitial sites, i.e. varying Pt/C ratios. Although all crystal structures of Pt–C used for reference are characterized by a nominal 1:1 Pt-to-C ratio, the actual carbon content within an individual Pt NP may differ. Furthermore, the presence of a small crystalline Pt core or residues of pure Pt cannot be ruled out completely. This would lead to localised carbon gradients, resulting in strain and distortion.

After activation, at early stages and after three days at reaction conditions, NPs were occasionally observed to be covered by layers of graphitic carbon of varying thicknesses (Figure 5a–c). This unwanted build-up of graphitic carbon, the so-called catalyst coking, has been previously described as the major cause for catalyst deactivation.[13] The increase of coking with time at reaction condition and the presence of coking from the early stages of the reaction indicates that improving the formation of propylene by carbon ordering in the Pt NPs is a delicate balancing act—leading to enhanced propylene production at lower quantities while causing catalyst coking at larger contents.

DFT Calculations

Next, the role of the ordered Pt–C solid solutions in PDH was investigated using DFT simulations (details can be found in the SI). The computational simulations were performed using the Perdew–Burke–Ernzerhof (PBE) functional for propane and propylene dehydrogenation over clean Pt(110), Pt(110) with subsurface carbon.

In line with literature reports,[5a,19] it was found that propylene undergoes deep dehydrogenation on the Pt(110) due to the strong Pt–H interaction (Figure S10), which can cause the formation of carbon deposition on the surface as observed experimentally (Figure 5). Furthermore, it was observed that a small accumulation of subsurface C species in Pt reduces the activity of the Pt (110) surface (Figure S11). Despite the presence of subsurface C, the Pt (110) surface continued to accumulate carbon due to deep dehydrogenation.

Once sufficient carbon has been accumulated to drive a transition to Pt–C, the surface becomes more selective in dehydrogenation to propylene while the overall activity is reduced. DFT calculations have been further conducted on (110) terminated ZnS-type Pt–C polymorph as an example for Pt–C.

Propane dehydrogenation over (110) terminated ZnS-type Pt–C polymorph was found to begin by weak adsorption of propane, with an adsorption energy of 0.05 eV (shown in Figure 6a), much like the reactions on Pt (110).

Figure 6. Enhancement of propylene production of Pt–C polymorphs. a) Minimum energy paths for the dehydrogenation of propane over ZnS-type Pt–C polymorph(110) considered up to propylene dehydrogenation. The black path shows the dehydrogenation of propane and the blue path the dehydrogenation of the $C_3H_{7,ads}$ fragment and propylene desorption. The dashed path shows propylene dehydrogenation. (Grey spheres = Pt, black spheres = carbon, white spheres = hydrogen). b) Comparison of the energetics for propane adsorption (orange), bound propylene (red), and activation energies (E_a) for propylene dehydrogenation (blue) for clean Pt surfaces, Pt with subsurface C (Pt + C) and ordered Pt–C solid solutions (ZnS-type). c) calculated density of states (DOS) for different Pt–C structures and pure Pt.
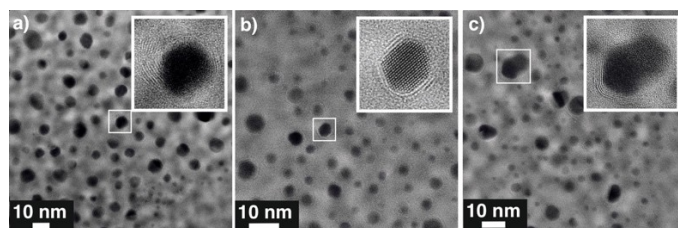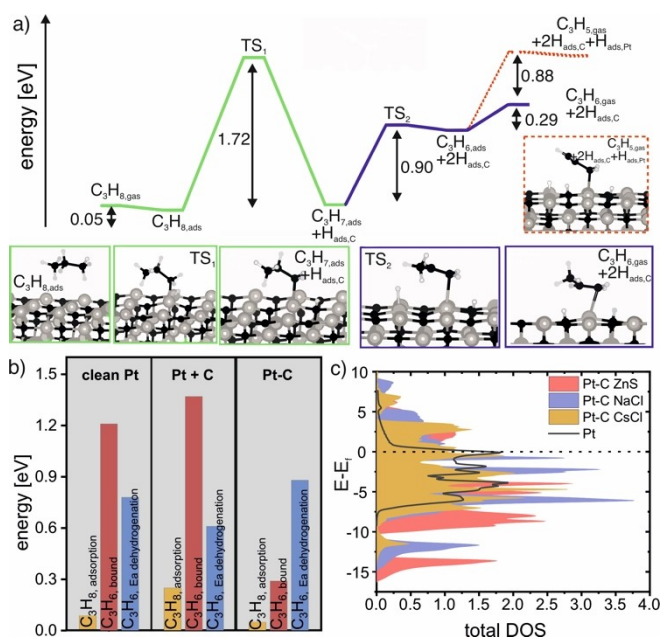

Figure 5. The unwanted build-up of graphitic carbon, catalyst coking, was observed at all stages of the reaction. a) TEM imaging of catalyst coking after activation, b) after 7 minutes and c) after 3 days at 600°C.

However, dehydrogenation of propane was found to be strongly activated on the Pt–C surface, with an activation energy of 1.72 eV for transferring hydrogen to a carbon site on the surface by breaking the C–H bond over Pt. Note that H adsorption on C sites is energetically favorable over adsorption on Pt sites despite Pt participating in bond rupture. This strong site preference makes adsorbed hydrogen relatively immobile, with a barrier for hopping from C to Pt of 1.43 eV. Thus, H_{ads} is expected to remain at the active site as the adsorbed $C_3H_{7,ads}$ fragment undergoes further reaction. In the second step of dehydrogenation on ZnS-type Pt–C polymorph, a second hydrogen atom is stripped from the $C_3H_{7,ads}$ fragment via a neighboring Pt atom through a process activated by 0.90 eV, see TS_2 in Figure 6a. This reaction leads to a second H_{ads} binding on the second C site at the active center. At this point, the two C atoms around the active Pt site are saturated with H_{ads} (see state labeled $C_3H_{6,ads}+2H_{ads,c}$ in Figure 6a). The product propylene is then bound by only 0.29 eV. This weak adsorption energy implies propylene will desorb rather than undergo further dehydrogenation, which has a barrier of 0.88 eV. Furthermore, re-absorption of propylene on the clean surface of the ZnS-type Pt–C polymorph has an adsorption energy of only 0.15 eV. Thus, propylene is not expected to undergo significant further reaction on the ZnS-type Pt–C polymorph. This situation can be contrasted with Pt(110) and Pt(110) with accumulated sub-surface carbon species (Figure 6b), where the bound energy of propylene is larger than the activation energy for dehydrogenation. Similarly, the (110) surface of the ZnS-type Pt–C polymorph without adsorbed carbon is expected to be ineffective in deep dehydrogenation owing to the large activation energy for dehydrogenation of propylene as compared to its adsorption energy (Figure S12). The weak adsorption of propylene on ZnS-type Pt–C polymorph is in line with theoretical data presented for PtZn alloys.[19] Furthermore, the ordering of C within the Pt bulk changes the electronic structure of the catalyst. As can be seen by the calculated density to states (DOS) presented in Figure 6c and Figure S13 within the different ordered Pt–C solid solutions the d-band center is shifted to more negative values compared to pure Pt implying a reduced activity, though the ordered Pt–C solid solutions remain metallic. Moreover, Bader charge calculations (Table S2) suggest covalent bonding contributions between Pt and C.

Discussion

This work highlights the importance of *operando* investigations in heterogeneous catalysis research. OTEM allowed us to identify the formation of ordered Pt–C solid solutions and correlate their roles to propylene formation during PDH. To the best of our knowledge no other *operando* TEM study of an endothermic dehydrogenation reaction has been reported. Our findings on the correlation of the diffusion of carbon into the catalyst with an increase in propylene production are in agreement with *ex situ* studies of PDH using Pt NPs.[20,21] Previous studies focusing on

dehydrogenation of hydrocarbons over Pt catalysts have shown that during the reaction at 420°C, carbon diffuses into the bulk of the catalyst and alters activity and selectivity.[12,22] Furthermore, the impure Pt was found to remain metallic.[12,23] However, the structure of these selective Pt–C compounds remained elusive until now. In addition, the observed onset temperature of enhanced propylene production (Figure 1) is in good agreement with published data.[12,22] Thus, the enhanced propylene production can be explained by the formation of ordered Pt–C solid solutions (Figure 2). Our findings suggest that this is due to the co-existence of different ordered Pt–C polymorphs at reaction conditions. As the observed structural changes occur in the same temperature regime compared to previous reports, we propose that the entire range of observed Pt–C polymorphs, which give rise to a more selective catalyst system, compose this previously unknown structure. This is also in agreement with previous reports showing that Pt–C solid solutions are beneficial for the catalytic hydrocarbon conversion.[11c]

Platinum Carbon Polymorphs

The diffusion of carbon into Pt NPs has previously been described as a prerequisite for Pt–C formation. Using EXAFS analysis of Pt NPs exposed to hydrocarbon atmospheres, a Pt:C ratio of 1 was proposed.[24] Among the huge variety of different Pt–C polymorphs, the ZnS-type Pt–C polymorph (2.05 Å) matched the reported Pt–C distances (1.94 Å[24a] to 2.02 Å[24b]) best. The ZnS-type Pt–C polymorph was also observed in our study at 600°C using SAED (Figure 2) and HRTEM (Figures 3 and 4). It should be noted that the energy barriers between different Pt–C polymorphs, in particular of the ZnS- and NaCl-type, are low and can easily be overcome even at room temperature.[17] Thus, positions of the carbon atoms could be fluctuating within the Pt lattice, leading to the coexistence of different Pt–C structures.[25] This hypothesis is supported by the SAED analysis conducted at 600°C during PDH. Since the time scale of catalytic reactions lies below the time resolution of our study and the SAED information is averaged over a larger region, rapidly fluctuating structures of the ZnS-type and NaCl-type Pt–C polymorphs may appear to coexist (Figure 2c).

The Effect of Platinum-Carbon Formation on Catalytic Performance

The *in situ* generated ordered Pt–C solid solutions are in dynamic exchange with the surface and can continuously modify the reactive interface. The ever-changing interface prevents that excessive surface tension kinetically inhibits dissolution and at the same time preserves the size of the lattice-distorted Pt (Figure S14). The "true" stoichiometry of the ordered Pt–C solid solution is adjusted by the local chemical potential of the gas phase and is, therefore, variable for different particles (Figure 3 and 4). We predict

that efficient reaction control will depend very sensitively on minute details of the real structure and the chemistry of the Pt nanoparticle. The intercalation of carbon into the bulk of Pt can also explain the detrimental effect of oxygen during regeneration.[26] By destroying the Pt–C system, oxygen causes a re-structuring of the nanoparticle, which changes the kinetics of heteroatom uptake in subsequent PDH cycles to ultimately reduce the efficiency of the catalytic process.

The observed carbon diffusion, structural fluctuations, and the coexistence of different Pt–C polymorphs form the ideal basis for the occurrence of frustrated phase transitions. Frustrated phase transitions can maintain high catalytic activity,[27] or moderate selectivity.[28] The observed coexistence of different Pt–C structures (Figure 2b) may originate from fast structural fluctuations leading to structural strain and therefore to the occurrence of frustrated phase transitions enhancing the olefine production. Thus, the frustrated phase transition stemming from the interconversion of the ZnS-type to the NaCl-type Pt–C polymorphs may be an important selectivity moderator at high temperatures. Especially, as carbon diffusion onto different interstitial sites in Pt has been reported to be fast.[17] Consequently, the existence of Pt–C polymorphs when propylene production is high, might be crucial for continuous catalyst operation under PDH conditions. The CsCl-type Pt–C polymorph observed *in situ* could initiate and accelerate the propylene production in the temperature regime around 450 °C, which is high enough to enable Pt bulk diffusion of heteroatoms as demonstrated previously.[27]

We hypothesize that the nobility of Pt is the driving force that transforms Pt into a highly productive and universal thermal gas phase catalyst. "Sensing" the presence of heteroatoms in the bulk can keep the Pt in an excited, metastable and thermodynamically frustrated state.

The Effect of Platinum-Carbon Formation on Coking

For PDH catalysts coking is the main source of deactivation. Coke was found to be present from the early stages of the reaction (Figure 5), which is in line with literature reports stating that pure Pt surfaces are covered by one or multiple layers after exposure to hydrocarbons.[29] We observed that Pt–C NPs appear more roundish compared to the metallic Pt. This is in agreement that high indexed surfaces are needed to activate the hydrocarbon and to pursue carbon subduction.[20b,29–30] Transport of carbon on transition metal surfaces can involve different mechanisms, including desorption, migration, and bulk diffusion.[31]

We propose that the coke detected in our study, formed via different mechanisms: At the early stages of the reaction, the coke formed directly on the surface of Pt nanoparticles due to deep dehydrogenation (Figure 5b). This way carbon accumulates at the surface of the nanoparticle and prevents the particle from taking part in the catalytic process. This self-limiting process depends on the availability of free low index Pt surfaces[29–31] and promotes graphitic carbon growth.[32] Secondly, carbon species could intercalate in the bulk of some NPs (Figure 2), which in its early stages can

lead to increased propylene production. With time on stream the carbon content in the bulk in some particles can supersaturate locally to ultimately lead to the nucleation of graphitic carbon at the surface. The latter might lead to the formation of graphitic carbon structures, including the formation of carbon nanotubes (CNTs) over time (Figure S15).[31,33] Both coking mechanisms can cause deactivation (for further details we refer to the Supporting Information).

On the General Effect of Heteroatom Intercalation into Pt during PDH

Here we showed the importance of carbon diffusion and the formation of ordered Pt–C solid solutions to the propylene formation in PDH. This is in agreement with findings relating to the role of alloys and intermetallic compounds on the production of highly efficient PDH Pt- based catalysts.[1] Alloying synergistically combines a catalytically active noble metal and a heteroelement, such as Zn, In, Mn or Sn, and leads to an increase in selectivity of the dehydrogenation product and an increase in activity.[4b,7] Similar to our study, selective Pt–X alloys (X=heteroelement) can be generated during an activation period under reaction conditions.[5a] Alloying alters the geometric (i.e. site isolation) and electronic (i.e. d-band shift) structures of the catalyst,[34] leading to modified reactivity. The d-band shift, site isolation and reactivity changes are in line with our DFT results on selectivity enhancement (Figure 6a,b) and the calculated DOS of the Pt–C polymorphs (Figure 6c, Figure S13).

Many intermetallic compounds formed during the dehydrogenation reaction correspond to the CuAu or Cu$_3$Au structures.[6,8,35] It was found that composites with a noble metal-to-heteroatom ratio of 1:1 are more selective compared to those with a ratio of 3:1.[36] In addition, for the intermetallic phase PdIn, the CsCl-type crystal structure was found to be highly selective.[37] Our observed self-doping of Pt by carbon suggests that the formation of simple intermetallic compounds is a general necessity for productivity enhancement in dehydrogenation catalysts. This further supports our finding that the chemistry and fluctuating nature of Pt–C polymorphs play a crucial role in enhancing the propylene production (see Figure 1, Figure 2). We foresee that the lifetime of Pt-based PDH catalyst can be extended by promoting the carbon diffusion within the Pt nanoparticle. Simultaneously, the saturation of Pt NPs by carbon and the nucleation of carbon sites on the surface of Pt NPs would have to be avoided. We hypothesize that this challenging endeavour could be accomplished by avoiding the local cooling of active sites during the endothermic PDH reaction. This could be achieved by continuous cofeeding or pulsing trace amounts of mild oxidants to remove carbon nuclei at the surface of Pt NPs *in situ*, without affecting the Pt–C solid solution. Further studies are needed to understand the influence of alloy, particle sizes, support, and promoters on the formation of Pt–C solid solutions.

Conclusion

In summary, we have shown that *operando* TEM delivers meaningful insights into the working structure of Pt catalysts for the industrially relevant reaction of PDH by correlating structure with catalyst activity. The diffusion of carbon into the Pt structure and the formation of Pt–C polymorphs have been found to play a crucial role in PDH. The *in situ* formation of the Pt–C polymorphs correlated with a change in the productivity towards propylene. Furthermore, HRTEM imaging and IFFT analysis revealed the presence of heavily strained NPs and the coexistence of multiple structures in individual NPs leading to local strain and frustrated phase transitions between the ZnS-type, NaCl-type and CsCl-type Pt–C polymorphs. Computational analysis using DFT of the Pt–C structures showed that carbon ordering on interstitial sites of Pt reduces the activity and affinity for adsorption of propylene and prevents deep dehydrogenation. Our *operando* TEM work, thus, contributes directly to the understanding of what structures constitute an active, highly selective catalyst dehydrogenation reactions. These results unlock a deeper understanding of the mechanisms driving PDH, leading us a step closer to realizing the ultimate goal of smart, tailored catalyst design.

Supporting Information

The authors have cited additional references within the Supporting Information.[38-48]

Conflict of Interest

The authors declare no conflict of interest.

Data Availability Statement

The data that support the findings of this study are openly available in AC/CatLab Archive at https://ac.archive.fhi.mpg.de/P52017, reference number P52017.

Keywords: *operando* TEM · industrial catalysis · electron diffraction · heterogeneous catalysis · solid solution

[1] S. Chen, X. Chang, G. Sun, T. Zhang, Y. Xu, Y. Wang, C. Pei, J. Gong, *Chem. Soc. Rev.* **2021**, *50*, 3315–3354.

[2] Bloomberg, K. Research, S. estimates, Statista **2020**.

[3] J. J. H. B. Sattler, J. Ruiz-Martinez, E. Santillan-Jimenez, B. M. Weckhuysen, *Chem. Rev.* **2014**, *114*, 10613–10653.

[4] a) M. D. Argyle, C. H. Bartholomew, *Catalysts* **2015**, *5*, 145–269; b) L. Rochlitz, Q. Pessemesse, J. W. A. Fischer, D. Klose, A. H. Clark, M. Plodinec, G. Jeschke, P.-A. Payard, C. Copéret, *J. Am. Chem. Soc.* **2022**, *144*, 13384–13393.

[5] a) H. Xiong, S. Lin, J. Goetze, P. Pletcher, H. Guo, L. Kovarik, K. Artyushkova, B. M. Weckhuysen, A. K. Datye, *Angew. Chem. Int. Ed.* **2017**, *56*, 8986–8991; b) H. N. Pham, J. J. H. B. Sattler, B. M. Weckhuysen, A. K. Datye, *ACS Catal.* **2016**, *6*, 2257–2264.

[6] P. Ingale, K. Knemeyer, P. Preikschas, M. Ye, M. Geske, R. Naumann d'Alnoncourt, A. Thomas, F. Rosowski, *Catalysis Science, Technology* **2021**, *11*, 484–493.

[7] Z. Lian, C. Si, F. Jan, S. Zhi, B. Li, *ACS Catal.* **2021**, *11*, 9279–9292.

[8] E. C. Wegener, Z. Wu, H.-T. Tseng, J. R. Gallagher, Y. Ren, R. E. Diaz, F. H. Ribeiro, J. T. Miller, *Catal. Today* **2018**, *299*, 146–153.

[9] V. Ponec, *Polyhedron* **1988**, *7*, 2383–2386.

[10] D. Zhao, X. Tian, D. E. Doronkin, S. Han, V. A. Kondratenko, J.-D. Grunwaldt, A. Perechodjuk, T. H. Vuong, J. Rabeah, R. Eckelt, U. Rodemerck, D. Linke, G. Jiang, H. Jiao, E. V. Kondratenko, *Nature* **2021**, *599*, 234–238.

[11] a) Y. Sun, Y. Cao, L. Wang, X. Mu, Q. Zhao, R. Si, X. Zhu, S. Chen, B. Zhang, D. Chen, Y. Wan, *Nat. Commun.* **2020**, *11*, 4600; b) D. Teschner, J. Borsodi, A. Wootsch, Z. Révay, M. Hävecker, A. Knop-Gericke, S. D. Jackson, R. Schlögl, *Science* **2008**, *320*, 86–89; c) J. Shan, H. Wang, P. Yoo, H. Nguyen, F.-K. Chiang, P. Liao, J. Cheng, *ACS Materials Lett.* **2021**, *3*, 179–186.

[12] Z. Paál*, Z. Zhaoqi, I. Manniger, M. Muhler, *Appl. Catal.* **1990**, *66*, 301–317.

[13] C. H. Bartholomew, *Appl. Catal. A* **2001**, *212*, 17–60.

[14] Y. Niu, X. Huang, Y. Wang, M. Xu, J. Chen, S. Xu, M.-G. Willinger, W. Zhang, M. Wei, B. Zhang, *Nat. Commun.* **2020**, *11*, 3324.

[15] M. T. Greiner, J. Cao, T. E. Jones, S. Beeg, K. Skorupska, E. A. Carbonio, H. Sezen, M. Amati, L. Gregoratti, M. G. Willinger, A. Knop-Gericke, R. Schlogl, *ACS Catal.* **2018**, *8*, 2286–2295.

[16] R. Schlögl, *ChemCatChem* **2017**, *9*, 533–541.

[17] Q. Li, X. Zhang, H. Liu, H. Wang, M. Zhang, Q. Li, Y. Ma, *Inorg. Chem.* **2014**, *53*, 5797–5802.

[18] a) K. Lu, C.-F. Huo, Y. He, J. Yin, J. Liu, Q. Peng, W.-P. Guo, Y. Yang, Y.-W. Li, X.-D. Wen, *J. Phys. Chem. C* **2018**, *122*, 23191–23199; b) Y. Bleu, V. Barnier, F. Christien, F. Bourquard, A. S. Loir, F. Garrelie, C. Donnet, *Carbon* **2019**, *155*, 410–420.

[19] S. Chen, Z.-J. Zhao, R. Mu, X. Chang, J. Luo, S. C. Purdy, A. J. Kropf, G. Sun, C. Pei, J. T. Miller, X. Zhou, E. Vovk, Y. Yang, J. Gong, *Chem* **2021**, *7*, 387–405.

[20] a) S. Vajda, M. J. Pellin, J. P. Greeley, C. L. Marshall, L. A. Curtiss, G. A. Ballentine, J. W. Elam, S. Catillon-Mucherie, P. C. Redfern, F. Mehmood, P. Zapol, *Nat. Mater.* **2009**, *8*, 213; b) J. Zhu, M.-L. Yang, Y. Yu, Y.-A. Zhu, Z.-J. Sui, X.-G. Zhou, A. Holmen, D. Chen, *ACS Catal.* **2015**, *5*, 6310–6319.

[21] W. Zhang, H. Wang, J. Jiang, Z. Sui, Y. Zhu, D. Chen, X. Zhou, *ACS Catal.* **2020**, *10*, 12932–12942.

[22] Z. Paál, H. Groeneweg, J. Paál-Lukács, *J. Chem. Soc. Faraday Trans.* **1990**, *86*, 3159–3166.

[23] Z. Paál, U. Wild, A. Wootsch, J. Find, R. Schlögl, *Phys. Chem. Chem. Phys.* **2001**, *3*, 2148–2155.

[24] a) A. Caballero, F. Villain, H. Dexpert, F. LePeltier, J. Lynch, *J. Chem. Soc. Faraday Trans.* **1993**, *89*, 159–164; b) N. S. Guyot-Sionnest, F. Villain, D. Bazin, H. Dexpert, F. Le Peltier, J. Lynch, J. P. Bournonville, *Catal. Lett.* **1991**, *8*, 283–295.

[25] D. F. Ogletree, M. A. van Hove, G. A. Somorjai, *Surf. Sci.* **1987**, *183*, 1–20.

[26] A. Iglesias-Juez, A. M. Beale, K. Maaijen, T. C. Weng, P. Glatzel, B. M. Weckhuysen, *J. Catal.* **2010**, *276*, 268–279.

[27] M. Plodinec, H. C. Nerl, F. Girgsdies, R. Schlögl, T. Lunkenbein, *ACS Catal.* **2020**, *10*, 3183–3193.

[28] M. T. Greiner, T. E. Jones, A. Klyushin, A. Knop-Gericke, R. Schlögl, *J. Am. Chem. Soc.* **2017**, *139*, 11825–11832.

[29] S. M. Davis, F. Zaera, G. A. Somorjai, *J. Catal.* **1982**, *77*, 439–459.

[30] M. C. Tsai, E. L. Muetterties, *J. Am. Chem. Soc.* **1982**, *104*, 2534–2539.

[31] A. Y. Tontegode, *Prog. Surf. Sci.* **1991**, *38*, 201–429.

[32] a) R. S. Weatherup, A. J. Shahani, Z.-J. Wang, K. Mingard, A. J. Pollard, M.-G. Willinger, R. Schloegl, P. W. Voorhees, S. Hofmann, *Nano Lett.* **2016**, *16*, 6196–6206; b) Z.-J. Wang, J. Dong, Y. Cui, G. Eres, O. Timpe, Q. Fu, F. Ding, R. Schloegl, M.-G. Willinger, *Nat. Commun.* **2016**, *7*, 13256.

[33] H. C. Nerl, M. Plodinec, *Microsc. Microanal.* **2022**, *28*, 1864–1865.

[34] Y. Nakaya, F. Xing, H. Ham, K.-i. Shimizu, S. Furukawa, *Angew. Chem. Int. Ed.* **2021**, *60*, 19715–19719.

[35] a) V. J. Cybulskis, B. C. Bukowski, H.-T. Tseng, J. R. Gallagher, Z. Wu, E. Wegener, A. J. Kropf, B. Ravel, F. H. Ribeiro, J. Greeley, J. T. Miller, *ACS Catal.* **2017**, *7*, 4173–4181; b) L. G. Cesar, C. Yang, Z. Lu, Y. Ren, G. Zhang, J. T. Miller, *ACS Catal.* **2019**, *9*, 5231–5244.

[36] S. C. Purdy, R. R. Seemakurthi, G. M. Mitchell, M. Davidson, B. A. Lauderback, S. Deshpande, Z. Wu, E. C. Wegener, J. Greeley, J. T. Miller, *Chem. Sci.* **2020**, *11*, 5066–5081.

[37] Z. Wu, E. C. Wegener, H.-T. Tseng, J. R. Gallagher, J. W. Harris, R. E. Diaz, Y. Ren, F. H. Ribeiro, J. T. Miller, *Catalysis Science, Technology* **2016**, *6*, 6965–6976.

[38] S. B. Vendelbo, C. F. Elkjær, H. Falsig, I. Puspitasari, P. Dona, L. Mele, B. Morana, B. J. Nelissen, R. van Rijn, J. F. Creemer, P. J. Kooyman, S. Helveg, *Nat. Mater.* **2014**, *13*, 884.

[39] M. Plodinec, H. C. Nerl, R. Farra, M. G. Willinger, E. Stotz, R. Schlögl, T. Lunkenbein, *Microsc. Microanal.* **2020**, *26*, 220–228.

[40] B. Fritsch, M. Wu, A. Hutzler, D. Zhou, R. Spruit, L. Vogl, J. Will, H. Hugo Pérez Garza, M. März, M. P. M. Jank, E. Spiecker, *Ultramicroscopy* **2022**, *235*, 113494.

[41] L. P. René de Cotret, M. R. Otto, M. J. Stern, B. J. Siwick, *Advanced Structural and Chemical Imaging* **2018**, *4*, 11.

[42] L. P. René de Cotret, B. J. Siwick, *Struct. Dyn.* **2016**, *4*.

[43] a) P. Giannozzi, S. Baroni, N. Bonini, M. Calandra, R. Car, C. Cavazzoni, D. Ceresoli, G. L. Chiarotti, M. Cococcioni, I. Dabo, A. Dal Corso, S. de Gironcoli, S. Fabris, G. Fratesi, R. Gebauer, U. Gerstmann, C. Gougoussis, A. Kokalj, M. Lazzeri, L. Martin-Samos, N. Marzari, F. Mauri, R. Mazzarello, S. Paolini, A. Pasquarello, L. Paulatto, C. Sbraccia, S. Scandolo, G. Sclauzero, A. P. Seitsonen, A. Smogunov, P. Umari, R. M. Wentzcovitch, *J. Phys. Condens. Matter* **2009**, *21*, 395502; b) P. Giannozzi, O. Andreussi, T. Brumme, O. Bunau, M. Buongiorno Nardelli, M. Calandra, R. Car, C. Cavazzoni, D. Ceresoli, M. Cococcioni, N. Colonna, I. Carnimeo, A. Dal Corso, S. de Gironcoli, P. Delugas, R. A. DiStasio, A. Ferretti, A. Floris, G. Fratesi, G. Fugallo, R. Gebauer, U. Gerstmann, F. Giustino, T. Gorni, J. Jia, M. Kawamura, H. Y. Ko, A. Kokalj, E. Küçükbenli, M. Lazzeri, M. Marsili, N. Marzari, F. Mauri, N. L. Nguyen, H. V. Nguyen, A. Otero-de-la-Roza, L. Paulatto, S. Poncé, D. Rocca, R. Sabatini, B. Santra, M. Schlipf, A. P. Seitsonen, A. Smogunov, I. Timrov, T. Thonhauser, P. Umari, N. Vast, X. Wu, S. Baroni, *J. Phys. Condens. Matter* **2017**, *29*, 465901.

[44] J. P. Perdew, K. Burke, M. Ernzerhof, *Phys. Rev. Lett.* **1996**, *77*, 3865–3868.

[45] A. Dal Corso, *Comput. Mater. Sci.* **2014**, *95*, 337–350.

[46] N. Marzari, D. Vanderbilt, M. C. Payne, *Phys. Rev. Lett.* **1997**, *79*, 1337–1340.

[47] S. M. Davis, F. Zaera, G. A. Somorjai, *J. Catal.* **1982**, *77*, 439–459.

[48] N. M. Rodriguez, P. E. Anderson, A. Wootsch, U. Wild, R. Schlögl, Z. Paál, *J. Catal.* **2001**, *197*, 365–377.